HHS Public Access

Author manuscript

Adv Mater. Author manuscript; available in PMC 2019 February 01.

Published in final edited form as:

Adv Mater. 2018 February ; 30(6): . doi:10.1002/adma.201704367.

Activatable Hybrid Nanotheranostics for Tetramodal Imaging and Synergistic Photothermal/Photodynamic Therapy

Dr. Shreya Goel,
Department of Materials Science and Engineering, University of Wisconsin - Madison, USA 53705

Carolina A. Ferreira,
Department of Biomedical Engineering, University of Wisconsin - Madison, USA 53705

Dr. Feng Chen,
Department of Radiology, University of Wisconsin - Madison, USA 53705

Dr. Paul A. Ellison,
Department of Medical Physics. University of Wisconsin - Madison, USA 53705

Cerise M. Siamof,
Department of Radiology, University of Wisconsin - Madison, USA 53705

Dr. Todd E. Barnhar, and
Department of Medical Physics. University of Wisconsin - Madison, USA 53705

Prof. Weibo Cai
Department of Materials Science and Engineering, University of Wisconsin - Madison, USA 53705

Department of Biomedical Engineering, University of Wisconsin - Madison, USA 53705

Department of Radiology, University of Wisconsin - Madison, USA 53705

Department of Medical Physics. University of Wisconsin - Madison, USA 53705

University of Wisconsin Carbone Cancer Center, Madison, Wisconsin, USA 53705

Abstract

A novel, biocompatible, hybrid nanoplatform is developed to seek and treat cancer *in vivo*. [^{89}Zr]-labeled HMSN shell, CuS nanosatellites and photosensitizer porphyrin, self-assemble into a high-performance nanotheranostic agent that integrates positron emission tomography, fluorescence, Cerenkov Luminescence and Cerenkov Radiation Energy Transfer-based imaging, and, on-demand photothermal/photodynamic therapy. Localized and synergistic phototherapy shows complete tumor eradication with no recurrence or long-term toxicity.

Graphical abstract

Correspondence to: Weibo Cai.

Supporting Information

Supporting Information is available from the Wiley Online Library or from the author.

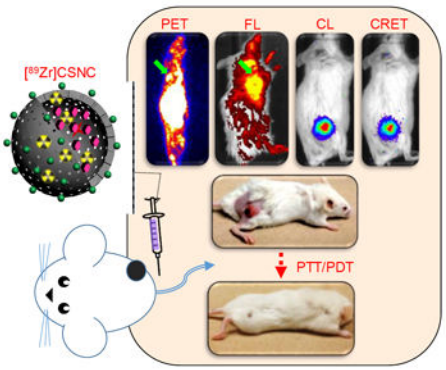

Keywords

core-satellite nanoparticles; multimodal imaging; synergistic therapy; cancer theranostics

A multifunctional core-satellite nanoconstruct (CSNC) is designed by assembling CuS nanoparticles on the surface of [^{89}Zr]-labeled hollow mesoporous silica nanoshells filled with porphyrin molecules, for effective cancer imaging and therapy. The hybrid nanotheranostic demonstrates three significant features: (1) simple and robust construction from biocompatible building blocks, demonstrating prolonged blood retention, enhanced tumor accumulation and minimal long-term systemic toxicity, (2) rationally selected functional moieties that interact together to enable simultaneous tetramodal (PET/FL/CL/CRET) imaging for rapid and accurate delineation of tumors and multimodal image-guided therapy *in vivo*, and (3) synergistic interaction between CuS-mediated photothermal therapy and porphyrin-mediated photodynamic therapy which results in complete tumor elimination within a day of treatment with no visible recurrence or side-effects. Overall, this proof-of-concept study illustrates an efficient, generalized approach to design high performance core-satellite nanohybrids that can be easily tailored to combine a wide variety of imaging and therapeutic modalities for improved and personalized cancer theranostics in the future.

Despite significant advances in our understanding of cancer biology and development of new therapies, survival rates for several common cancers remain unchanged. Tumor heterogeneity, growing incidences of drug resistance, and limited success of monotherapies in the clinic, have spurred the rapid development of combinatorial nanomedicine as a disruptive, yet effective alternative to traditional therapy.[1] Owing to non-specificity of chemotherapy which raises toxicity concerns, nanoparticle-mediated focal treatment paradigms such as photothermal therapy (PTT) and photodynamic therapy (PDT) have gained much traction recently.[2] Phototherapeutic agents that boast of non-invasive and stimuli-responsive nature, low systemic toxicity, and photo-irradiation-dependent tumor selectivity are rapidly gaining acceptance with several clinical trials on the way.[3, 4] However, limited tissue penetration depth and suboptimal performance of commonly used photosensitizers and transducers, have severely impeded therapeutic outcomes, encouraging the development of combination protocols that can afford enhanced, synergistic effects.

On the other hand, biomedical imaging has become the cornerstone of modern oncology, encouraging innovation beyond traditional contrast agents for faster, more efficient and robust diagnoses.[5] Rapid development of hybrid clinical scanners such as positron emission tomography (PET)/computed tomography (CT) and PET/magnetic resonance imaging (MRI), underscores the emerging importance of multimodality imaging that yields complementary anatomic, physiological and molecular information, not accessible by a single modality alone.[5] This has generated much interest in nanotracers that not only cater to these emerging technologies, but also enable patient screening and stratification, early lesion detection, image-guided therapy, treatment planning and monitoring.

Hybrid nanotheranostics aim to integrate the functionalities of their individual organic or inorganic building nanoblocks into a single, efficient, tunable and more effective system for combination imaging and therapy of cancer. Hence, it is essential to rationally select each component, design a module to seamlessly accommodate multiple diagnostic and therapeutic modalities, as well as optimize the trade-offs between performance enhancement and the ensuing structural and synthetic complexities. Yolk-shell nanostructures, the classical examples of multifunctional nanomaterials, are limited by complex and rigid synthetic chemistry, as well as suboptimal performance *in vivo*. Although researchers, including our group, have sought to alleviate the latter by injecting higher doses or introducing specific targeting ligands for enhanced tumor accumulation, such strategies only achieve partial success and add more layers of complexity to an already complex process.[6] This work adopts a straightforward approach to develop a highly efficient multimodal nanotheranostic by facile self-assembly of simpler components. Core-satellite nanoconstructs (CSNC) were prepared by assembling radiolabeled hollow mesoporous silica (HMSN), *meso*-tetrakis(4-carboxyphenyl)porphyrin (TCPP) and copper sulfide (CuS) nanoparticles, such that the hollow interior of each HMSN was filled with TCPP molecules and its exterior decorated with thousands of CuS nanosatellites. (Scheme 1)

HMSN, as an excipient not only enhances solubilization and hence, bioavailability of highly hydrophobic TCPP, but also helps in improving blood residence and thus, tumor accumulation of ultrasmall CuS, which otherwise clears rapidly *via* renal and hepatic pathways. Additionally, HMSN was used for chelator-free labeling with zirconium-89 (^{89}Zr, $t_{1/2}$ = 78.4 h) for PET and Cerenkov luminescence (CL) imaging.[7] TCPP encapsulated in HMSN served as a biocompatible, on-site activatable photodynamic agent for singlet oxygen-mediated destruction of tumor tissues.[8,9] Its intrinsic fluorescence (FL) and the ability to couple with the radionuclide for Cerenkov radiation energy transfer (CRET), were tapped for *in vivo* optical imaging. Dependence on photon emission during radioactive decay greatly serves to diminish autofluorescence in CL and CRET, and thereby improves the tumor-to-background contrast. Semiconductor CuS nanocrystals have been extensively explored as hyperthermia mediators owing to their high photothermal conversion efficiency[10], that is independent of nanoparticle size and surrounding media, photostability and low cytotoxicity, and were thus chosen for PTT in this study.[11, 12] Overall, hybrid CSNCs demonstrate three important properties, which also form the rationale behind the design: (1) Facile self-assembly of simple, non-toxic components that interact together to produce a high-performance, multifunctional yet highly biocompatible nanosystem, (2) Integration of modalities with complementary advantages, such as high sensitivity and

quantitative nature of PET, high spatial resolution of FL and reduced autofluorescence and dependence on tissue penetration depth of CL and CRET imaging, into a single construct, and (3) Combination of rationally-selected therapeutic modules that act synergistically to completely eradicate cancer.

Synthesis of well-dispersed nanoparticles, preferably in the size range 50 – 200 nm with appropriate surface modification is the key to achieving optimal pharmacokinetics *in vivo* i.e enhanced accumulation at the tumor site while prolonging blood circulation, evading opsonization by serum proteins and clearance by immune sentinels, the mononuclear phagocytic system.[13] HMSNs were synthesized by a modified three-step Stöber process as described earlier,[14] starting with synthesis of dense silica core, coating with mesoporous silica shell, followed by selective etching of the dense cores and amine modification to yield final HMSN-NH_2 cores. (Section S1, Supplementary Information) Citrate-capped negatively charged CuS nanoparticles were synthesized using well-established procedures, with minor modifications.[6, 11] Transmission electron microscopy (TEM) of HMSN and CuS-Cit nanoparticles indicated highly uniform, spherical morphology, with diameters ~ 150 nm and ~ 10 nm, respectively. (Figure 1a-b) Subsequently, HMSN_nCuS nanocomposites were prepared by electrostatic adsorption of negatively charged CuS-Cit on the surface of positively charged amine-modified HMSNs, employing different ratios by volume. (Figure S1) A final v/v ratio of 1:4 was selected for further studies, as a trade-off between CuS decoration density and colloidal stability, yielding a Cu/Si ratio of ≈ 0.08 (measured by microwave plasma atomic emission spectroscopy, Figure S1e) which yields ≈ 7833 CuS nanosatellites per HMSN core (Section S2, Supporting Information). The core-satellite morphology could be clearly visualized on TEM which indicated well-dispersed nanoparticles with narrow size distribution. (Figure 1c) Increase in hydrodynamic size (orange curve, Figure 1d) and reduction in ζ-potential from 47.8 ± 1.4 mV to 0.5 ± 0.1 mV (Figure 1d and S2a, respectively) confirmed successful attachment of CuS to HMSN. CuS nanosatellites were uniformly distributed in a monolayer and firmly bound to the HMSN shell. When incubated in high ionic strength physiological solutions at pH 5.5 or 7.4, CuS nanoparticles showed minimal detachment from HMSN even up to 24 h. (Figure S4, Supporting Information) CuS nanoparticles upon albumin interaction, are shown to assume a hydrodynamic size ~ 25 nm.[15] Absence of such a peak, as well as monomodal size distribution of HMSN_nCuS in DLS histograms confirmed the excellent stability of the nanoconstructs for further *in vivo* studies.

Poor water solubility of porphyrin severely impedes its biological applications, despite excellent photodynamic properties. HMSNs with high specific surface area and a large central cavity (~ 100 nm) make ideal nanocarriers for small molecule, hydrophobic drugs, and were specifically chosen to achieve maximal drug encapsulation and facile surface modification. Drug loading capacity of HMSN_nCuS was tested using both doxorubicin (DOX), a small-molecule model chemotherapeutic, as well as TCPP, and the influence of CuS adsorption on HMSN shell was evaluated by comparison with pristine HMSN-NH_2. As indicated in figure S2b, HMSN and HMSN_nCuS demonstrated no significant difference in loading capacity or efficiency for either DOX or TCPP. 640.80 ± 189.75 mg TCPP was loaded per gram of HMSN_nCuS (≈ 51.27 ± 14.35 % loading efficiency) to yield the final CSNCs. UV-Vis-NIR absorbance (Figure 1e) indicated that CSNCs retained the

characteristic absorbance peaks of TCPP and CuS and no significant attenuation was observed in the optical properties, thereby validating their application as combination PTT/PDT agents. Furthermore, slightly diminished fluorescence from TCPP encapsulated in HMSN_nCuS (owing to minor aggregation-induced quenching) could be rapidly reversed upon release of TCPP from the nanoconstructs. (Figure 1f) Branched polyethylene glycol ($SCM\text{-}PEG1_{0k}$) was grafted on the surface of as-prepared CSNCs to reduce aggregation and impart greater biocompatibility for *in vivo* applications. Successful PEGylation of CSNCs was confirmed by an increase in the hydrodynamic size (Figure 1d) and ζ-potential values. (Figure S2a) Moreover, $CSNC\text{-}PEG_{10k}$ demonstrated excellent colloidal stability upto 48 h in PBS. (Figure S3)

However, enhancement in photothermal performance is the key measure to validate the core-satellite design and its superiority over yolk-shell nanostructure (mesoporous silica shell-coated CuS; CuS@MSN). Accordingly, NIR photothermal conversion efficiency of HMSN_nCus was evaluated as a function of laser power density and irradiation time. (Figure S5, Supporting Information) and the hyperthermal effect was compared with CuS@MSN (Figure S6) As expected, HMSN_nCuS demonstrated much more rapid and larger overall change in temperature than CuS@MSN in response to irradiation with 980 nm laser (4 W cm^{-2}, 10 min). Subsequently, photothermal heating curves were determined for various nanoparticle solutions. Like CuS-Cit and HMSN_nCuS solutions, CSNCs too demonstrated a rapid but transient increase in temperature, (T_{max} > 45 °C, sufficient for hyperthermia-mediated tumor cell killing [3]), while water and HMSNs showed negligible variation. (Figure S5b and S5c) Furthermore, photodynamic property of CSNCs was evaluated by a singlet oxygen sensor green (SOSG) probe to quantify the release of reactive oxygen species (ROS) upon irradiation with ultra-red laser 660 nm (50 mW cm^{-2}, 20 min). [8] No significant difference was observed between photodynamic property of un-encapsulated TCPP control and CSNCs, demonstrated by rapid, time-dependent increase in SOSG fluorescence of the two solutions. (Figure S2c) Significantly lower (but not zero) ROS generation in pure HMSN_nCuS samples could be attributed to the weak photodynamic property of CuS nanoparticles as reported recently.[10] These encouraging results formed the basis for the subsequent *in vivo* synergistic phototherapy studies in murine breast tumor models.

An ideal nanotheranostic agent is one that can rapidly and accurately identify tumor location, define its morphology, and deliver therapy in a targeted fashion, leading to complete remission, with no relapse or side-effects.[16] Accordingly, CSNCs were evaluated as multimodal imaging agents, prior to their use for combination phototherapy. Intrinsically ^{89}Zr-labeled CSNCs were prepared by exploiting the oxophilicity of ^{89}Zr and abundant deprotonated silanol groups in HMSNs, as reported earlier by our group (section S1).[17] $HMSN\text{-}NH_2$ could be radiolabeled with high specificity and efficiency (Figure S2d) by simple incubation with [^{89}Zr]-oxalate in HEPES buffer (0.1 M, pH 7-8) for 2 h, followed by decoration with CuS nanosatellites, TCPP loading and PEG-modification as outlined before. End-of-synthesis radiolabeling yields after EDTA challenge were determined to be 94.5 ± 3.2 % and 73.1 ± 5.6 % at incubation temperatures of 70 °C and 37 °C, respectively. (Figure 1i) [^{89}Zr]$CSNC\text{-}PEG_{10k}$ prepared at 70 °C demonstrated excellent radiostability in simulated body fluid (Figure 1j), and was used for further *in vivo* investigation.

Subcutaneous 4T1 murine breast tumor-bearing mice were intravenously injected with [^{89}Zr]CSNC-PEG$_{10k}$ (7.4 MBq, corresponding to a dose of 2.5 mg kg^{-1} TCPP), to determine nanoparticle biodistribution and tumor-homing efficacy via serial PET and FL imaging. As shown in Figure 2a-b, [^{89}Zr]CSNC-PEG$_{10k}$ demonstrated prolonged blood residence, resulting in good tumor accumulation via the enhanced permeability and retention (EPR) effect. 3D region-of-interest (ROI) analysis on decay-corrected PET images indicated a gradual increase in tumor uptake upto 24 h post-injection (p.i.), reaching a maximum of 5.57 ± 0.71 percent injected dose per gram (%ID/g), followed by a slight decline to 4.90 ± 0.47 %ID/g, possibly due to the transient nature of the EPR effect. (Figure S7) FL imaging (Ex: 460 nm, Em: 720 nm) too demonstrated high tumor uptake, as well as high tumor-to-background contrast. (Figure 2c and S8a) *Ex vivo* biodistribution analysis performed 48 h p.i. after the final PET/FL scans validated the *in vivo* observations and corroborated well with the ROI analyses. (Figure S7d and S8b) *Ex vivo* FL imaging of tumor and major organs of uptake was also performed to better visualize CSNC biodistribution. (Figure 2d) Disparity in nanoparticle biodistribution profiles obtained via PET and FL imaging can be attributed to the limited tissue penetration of TCPP emission and further confirms the complementary advantages of multimodal imaging. While PET allows deep tissue imaging and more accurate evaluation of tracer pharmacokinetics, FL imaging can prove more useful for image-guided surgery and tumor resection. As a proof-of-concept of multimodality imaging, [^{89}Zr]CSNC-PEG$_{10k}$ was injected intratumorally in a separate cohort of mice and imaged consecutively using PET, FL, CL (Ex: closed, Em: open) and CRET (Ex: closed, Em: 720 nm). Strong, persistent signals were observed over two weeks of monitoring, indicating excellent potential of [^{89}Zr]CSNC-PEG$_{10k}$ as multimodal contrast agents. Good overlap of signals from the four imaging modalities at all time-points further validated the robust nature of the nanoconstructs. (Figure 2e-h and S9). Moreover, nearly consistent radioactive foci in PET images (Figure 2e) indicated minimal diffusion of CSNCs to the surrounding tissues, as well as excellent radiostability of ^{89}Zr *in vivo*. However, gradual diffusion of FL signal (Figure 2f) over time indicates successful release of TCPP cargo from CSNC. Interestingly, 4T1 tumors which typically grow 6-8 times their initial size within two weeks, showed visible retardation in further growth during the study period (seen clearly from PET/optical images in figure 2e-h). This exciting observation can be attributed to Cerenkov radiation induced photodynamic effect, and warrants in-depth investigation in the future.[9, 18]

Photothermally enhanced PDT has recently gained attention as a means to combat hypoxia-mediated resistance of tumors to PDT. However, majority of the reports involve photosensitizers anchored directly onto the individual photothermal nanoparticle (e.g. Au, graphene) with limited surface areas, resulting in sub-optimal loading and pre-mature release.[19] To evaluate the feasibility of using CSNCs for combination phototherapy *in vivo*, 4T1 tumor-bearing mice were randomized into 6 groups and administered various treatments as follows: (1) CSNC+PTT+PDT, (2) CSNC+PTT, (3) CSNC+PDT, (4) CSNC only, (5) PBS+PTT+PDT, and (6) PBS only. Experimental conditions were kept constant, i.e. 30 mg kg^{-1} intra-tumor dose of CSNCs; PTT via 980 nm laser irradiation (L_{980}, 4 W cm^{-2}, 10 min); PDT via 660 nm laser irradiation (L_{660}, 50 mW cm^{-2}, for 20 min). CSNC+NIR laser irradiation in groups 1 and 2 resulted in a rapid, local photothermal heating effect (T_{max} > 50 °C), compared to marginal temperature change in other groups. (Figure 3b) Tumor

volume, body weight and survival status of the mice were monitored regularly. Remarkably, 3 out of 5 mice in group 1 demonstrated complete eradication of the tumors within one day of treatment, and remaining two mice, by day 2. Continued monitoring over 30 days indicated complete healing of the irradiated area (Figure 3c), no relapse in tumor, steady movement and increasing body weight (Figure S10b), which significantly prolonged animal survival (Figure 3f). In contrast, groups receiving monotherapies (either PTT or PDT) demonstrated lower tumor growth inhibition rates (Figure S10a), showing an initial growth retardation upto day 7 post-treatment, after which tumors continued to grow, reaching 1.78±0.98 and 2.65±0.44 times the initial volumes, respectively. Of note, the interaction between PTT and PDT was found to be more effective than a purely additive one. As per Hahn's seminal work, cell survival after treatment with two mutually exclusive modalities (T_1 and T_2) can be calculated by multiplying the percentage of surviving cell population after T_1 with that after T_2.[20] When adapted to this study, average remaining tumor volumes in group 1 were found to be significantly smaller than predicted by Hahn's model, indicating a synergistic interplay between the two. (Figure 3g) Such synergism can be explained by possible improvement of tumor blood flow as a result of CuS-mediated hyperthermia, which in turn enhances oxygenation, and subsequently lessens tumor hypoxia, a major deterrent to PDT effectiveness.[19] Hence, overcoming hypoxia through focused hyperthermal reoxygenation is a promising strategy to enhance therapeutic outcomes. On the other hand, mice in the control groups failed to show any inhibition or retardation in tumor growth. (Figure 3e)

Hematoxylin and eosin (H&E) staining analysis of tumor tissues from different groups was carried out 15 days post-treatment. Owing to complete disappearance of tumors in mice of group 1, tumors from a separate set of treated mice were harvested at 6 h post-therapy. Figure 3d clearly demarcates the difference in tissue morphology between the various groups. Within 6 h post-treatment, group 1 demonstrated widespread tissue loss across large tumor areas, necrosis, and pyknosis in tumor cells undergoing apoptosis. Mice undergoing monotherapies demonstrated limited benefit, evident from the partial tissue damage and smaller necrotic regions interspersed with infiltrating tumor cells. Control groups showed minimal damage to the tumor tissues with thriving tumor cells and pleomorphic nuclei, indicating that both CSNC and laser irradiation are essential for effective tumor cell killing. In addition to effectiveness, biocompatibility is the most important requirement for a theranostic agent to be clinically relevant. To investigate whether CSNCs caused any detrimental effects in the long term, healthy mice were intravenously injected with a therapeutic dose (30 mg kg^{-1}) of CSNC-PEG_{10k} and monitored for two months. No noticeable toxic effects were observed, evidenced by similar morphology of H&E-stained liver and spleen tissues from CSNC and PBS-treated mice (Figure 3i), consistently increasing body weights and normal hematology reports. (Figure 4)

In conclusion, the present work demonstrated an optimized, multifunctional core-satellite nanotheranostic which integrates PET/FL/CL/CRET imaging and on-demand, focal photothermal and photodynamic therapies to seek and treat cancer *in vivo*. Enhanced hyperthermia and ROS production work together to produce a strong synergistic therapeutic effect, contributing to rapid and complete elimination of tumors *in vivo* with no recurrence or side-effects. Importantly, CSNCs were found to be highly biocompatible, as demonstrated

amply by long-term toxicological analysis. Overall, the work illustrates a generalized strategy for synthesis of core-satellite nanocomposites for multimodal image-guided combination therapy. Compared with yolk-shell nanostructures, CSNCs not only provide greater flexibility in selection of individual components and simpler synthetic chemistry, but also demonstrate enhanced performance by incorporating larger number of functional moieties per unit. As demonstrated already, DOX could be loaded inside our CSNCs with high efficiency, indicating the potential for trimodal chemo-/photothermal/photodynamic therapy. Photoaccoustic imaging capability of CuS can be further tapped to create a hyper-integrated all-in-one nanotheranostic in the near future. Moreover, the simple and robust design can be easily tailored for multitudinous applications. For example, by simply substituting CuS nanosatellites with Au or iron oxide nanoparticles, CSNCs can be endowed with NIRF, computed tomography (CT) and magnetic resonance imaging capabilities, respectively. Additionally, the HMSN shell can be tuned to radiolabel a variety of imaging and therapeutic isotopes such as $^{64}Cu(t_{1/2} = 12.8\ h)$ and ^{177}Lu ($t_{1/2} = 6.73\ d$), or deliver various cargos such as proteins, antibodies, genes, siRNA etc., promising exciting possibilities for hybrid nanotheranostics in the near future.

Supplementary Material

Refer to Web version on PubMed Central for supplementary material.

Acknowledgments

This work was supported, in part, by the University of Wisconsin - Madison, the National Institutes of Health (NIBIB/NCI 1R01CA169365, 1R01CA205101, 1R01EB021336, P30CA014520), and the American Cancer Society (125246-RSG-13-099-01-CCE).

References

1. He C, Lu J, Lin W. J Control Release. 2015; 219:224. [PubMed: 26387745]
2. Zhang Z, Wang J, Chen C. Adv Mater. 2013; 25:3869. [PubMed: 24048973]
3. Gao S, Zheng M, Ren X, Tang Y, Liang X. Oncotarget. 2016; 7:57367. [PubMed: 27384678]
4. Abbas M, Zou Q, Li S, Yan X. Adv Mater. 2017; 29:6.Zou Q, Abbas M, Zhao L, Li S, Shen G, Yan X. J Am Chem Soc. 2017; 139:1921. [PubMed: 28103663]
5. Goel S, England CG, Chen F, Cai W. Adv Drug Deliv Rev. 2016; 9:30233.
6. Chen F, Hong H, Goel S, Graves SA, Orbay H, Ehlerding EB, Shi S, Theuer CP, Nickles RJ, Cai W. ACS Nano. 2015; 9:3926. [PubMed: 25843647]
7. Goel S, Chen F, Luan S, Valdovinos HF, Shi S, Graves SA, Ai F, Barnhart TE, Theuer CP, Cai W. Adv Sci. 2016; 3
8. Yang G, Gong H, Qian X, Tan P, Li Z, Liu T, Liu J, Li Y, Liu Z. Nano Research. 2015; 8:751.
9. Kamkaew A, Cheng L, Goel S, Valdovinos HF, Barnhart TE, Liu Z, Cai W. ACS Appl Mater Interfaces. 2016; 8:26630. [PubMed: 27657487]
10. Wang S, Riedinger A, Li H, Fu C, Liu H, Li L, Liu T, Tan L, Barthel MJ, Pugliese G, DeDonato F, Scotto D'Abbusco M, Meng X, Manna L, Meng H, Pellegrino T. ACS Nano. 2015; 9:1788. [PubMed: 25603353]
11. Li Y, Lu W, Huang Q, Huang M, Li C, Chen W. Nanomedicine. 2010; 5:1161. [PubMed: 21039194]
12. Goel S, Chen F, Cai W. Small. 2014; 10:631. [PubMed: 24106015]
13. Blanco E, Shen H, Ferrari M. Nat Biotechnol. 2015; 33:941. [PubMed: 26348965]

14. Chen F, Hong H, Shi S, Goel S, Valdovinos HF, Hernandez R, Theuer CP, Barnhart TE, Cai W. Sci Rep. 2014; 4
15. Huang P, Li Z, Hu H, Cui D. J Nanomater. 2010; 2010:6.
16. Li X, Kim J, Yoon J, Chen X. Adv Mater. 2017; 29:29.
17. Chen F, Goel S, Valdovinos HF, Luo H, Hernandez R, Barnhart TE, Cai W. ACS Nano. 2015; 9:7950. [PubMed: 26213260]
18. Kotagiri N, Sudlow GP, Akers WJ, Achilefu S. Nat Nanotechnol. 2015; 10:370. [PubMed: 25751304]
19. Cheng L, Wang C, Feng L, Yang K, Liu Z. Chem Rev. 2014; 114:10869. [PubMed: 25260098]
20. Hahn GM, Braun J, Har-Kedar I. Proc Natl Acad Sci U S A. 1975; 72:937. [PubMed: 48253]

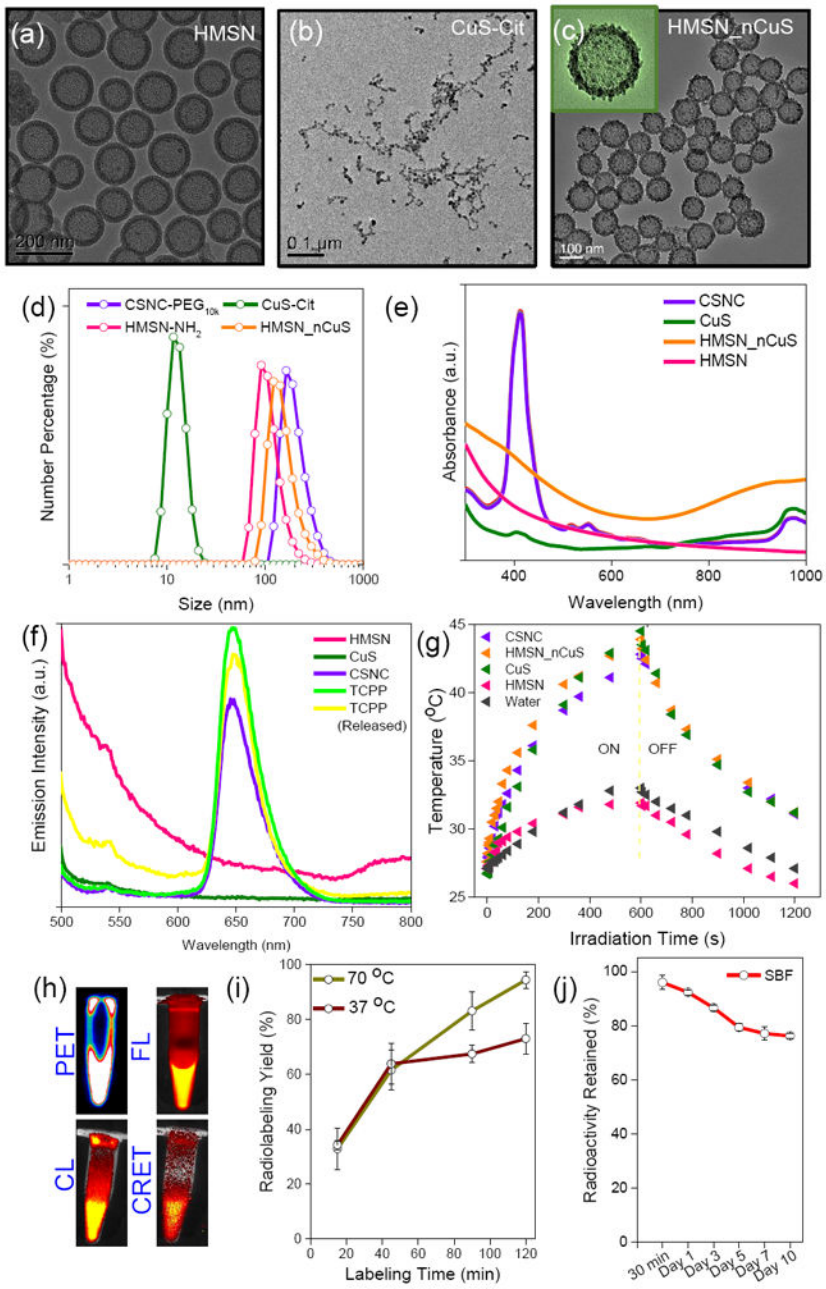

Figure 1. Characterization of CSNCs

(a-c) Transmission electron microscopy images of (a) HMSN, (b) CuS-Cit, and (c) HMSN_nCuS at different magnifications. (d) Hydrodynamic diameters measured via dynamic light scattering (DLS), and (e) UV-Vis-NIR spectra, of individual components and self-assembled CSNCs. (f) Emission spectra of different nanoparticle solutions and TCPP, based on fluorescence of TCPP (Ex: 420 nm). Encapsulation of TCPP into CSNC results in slight reduction in fluorescence (violet curve) possibly due to self-quenching. The fluorescence is rapidly regained upon release of TCPP from the nanoconstructs (yellow curve). (g) Time-dependent photothermal profiles of different nanoparticle solutions. (h) Representative PET, FL, CL and CRET images of radiolabeled CSNCs. (i) Time-dependent

chelator-free labeling of PET ^{89}Zr onto CSNCs at 37 and 70 °C after 50 mM EDTA challenge, and (j) radiostability of [^{89}Zr]CSNCs prepared at 70 °C in simulated body fluid over a period of 10 days.

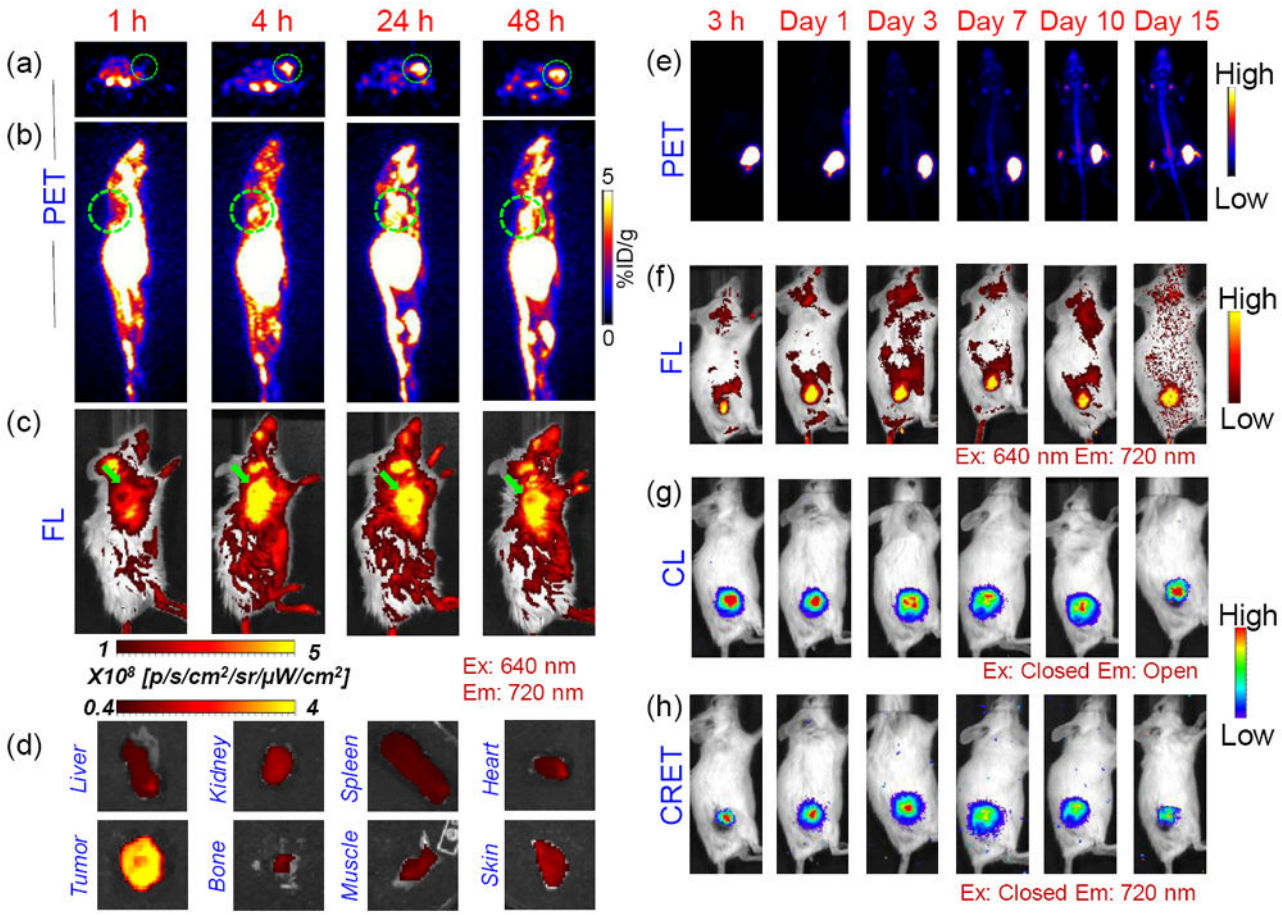

Figure 2. ***In vivo*** **multimodal imaging with [^{89}Zr]CSNC-PEG$_{10k}$**

Representative serial (a) axial PET slices, (b) sagittal maximum intensity projections (MIP) and (c) FL images overlaid with digital photographs depicting EPR-mediated uptake of intravenously injected [^{89}Zr]CSNC-PEG$_{10k}$ (~7.4 MBq; 2.5 mg kg^{-1} dose of TCPP) in 4T1 tumors (indicated by green circles and arrowheads) at 1, 4, 24 and 48 h p.i. (d) *Ex vivo* FL imaging of explanted tumor and major organs at 48 h p.i. (Ex: 640 nm, Em: 720 nm). (e) PET MIP images and optical (FL, CL and CRET) images of 4T1 tumor-bearing mice acquired at different time-points post-intratumor injection of [^{89}Zr]CSNC-PEG$_{10k}$ (~1.8 MBq; 0.7 mg kg^{-1} dose of TCPP). (n=3)

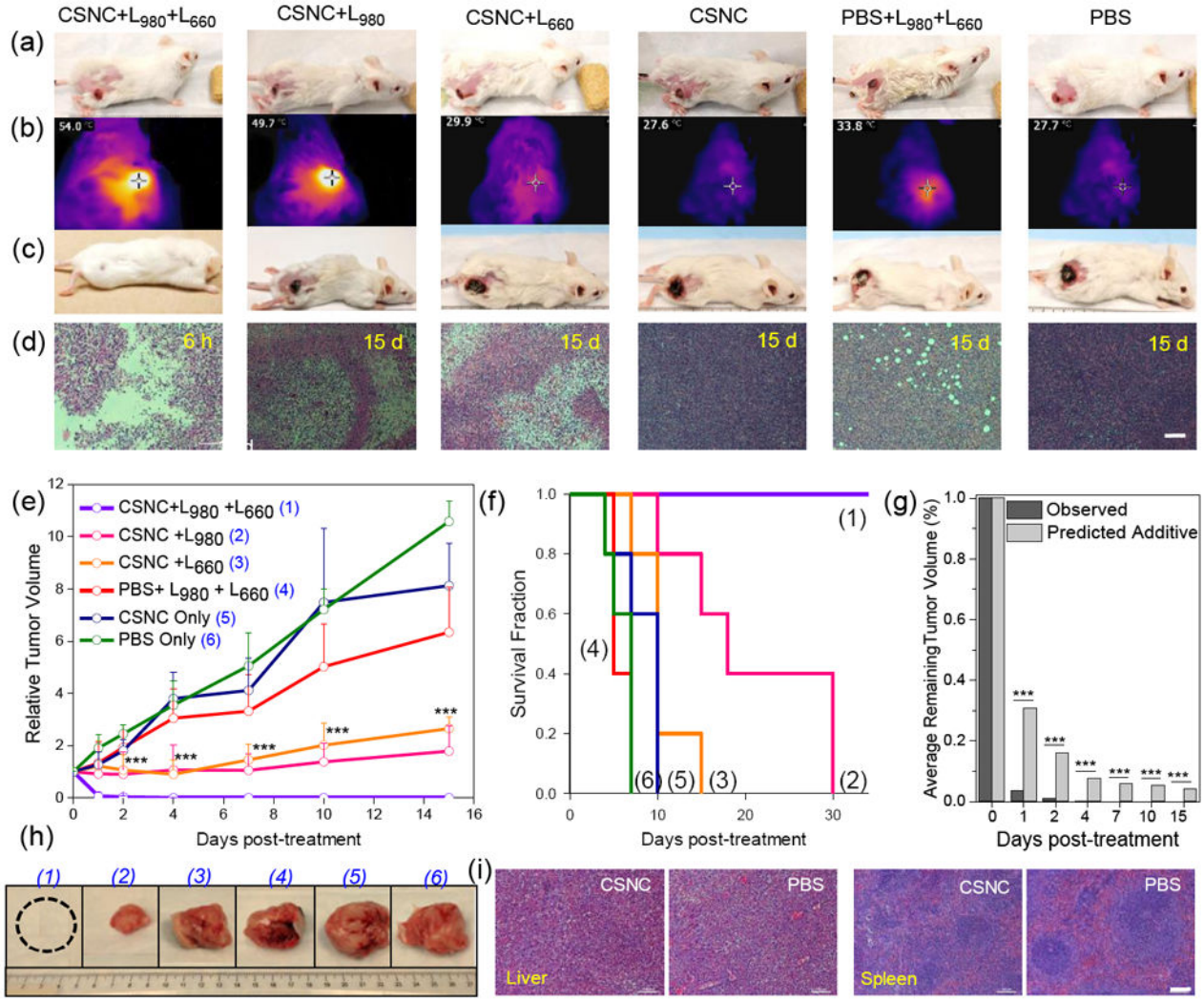

Figure 3. CSNC-mediated synergistic photothermal/photodynamic therapy *in vivo*

(a,c) Digital photographs of 4T1 tumor-bearing mice before and 15 days after different treatments. (b) IR thermal images depicting increase in temperature after irradiation with 980 nm laser. (d) H&E stained tumor sections collected 6 h or 15 days post-treatment. Scale bar: 100 μm. (e) Time-dependent tumor growth curves and (f) survival curves of mice after various treatments. (n = 5). (g) Synergistic behavior of CSNC-mediated PTT/PDT therapy indicated by a statistically significant difference between tumor volumes after dual-laser treatment and that predicted by a purely additive theoretical model. (h) Digital photographs of tumors explanted from different treatment groups 1-6, after 15 days. All experimental conditions were kept constant: CSNC dose: 30 mg kg^{-1}, 980 nm laser (4 W cm^{-2}) irradiated for 10 min followed by irradiation with 660 nm laser (50 $mWcm^{-2}$) for 20 min. Statistical analysis was performed using two sample t test (** $P < 0.01$, **** $P < 0.001$). (i) H&E stained slices of liver and spleen tissues explanted after 60 days from mice injected intravenously with therapeutic dose of CSNC-PEG_{10k} or PBS. Scale bar: 100 μm. Data presented as mean ± SD.

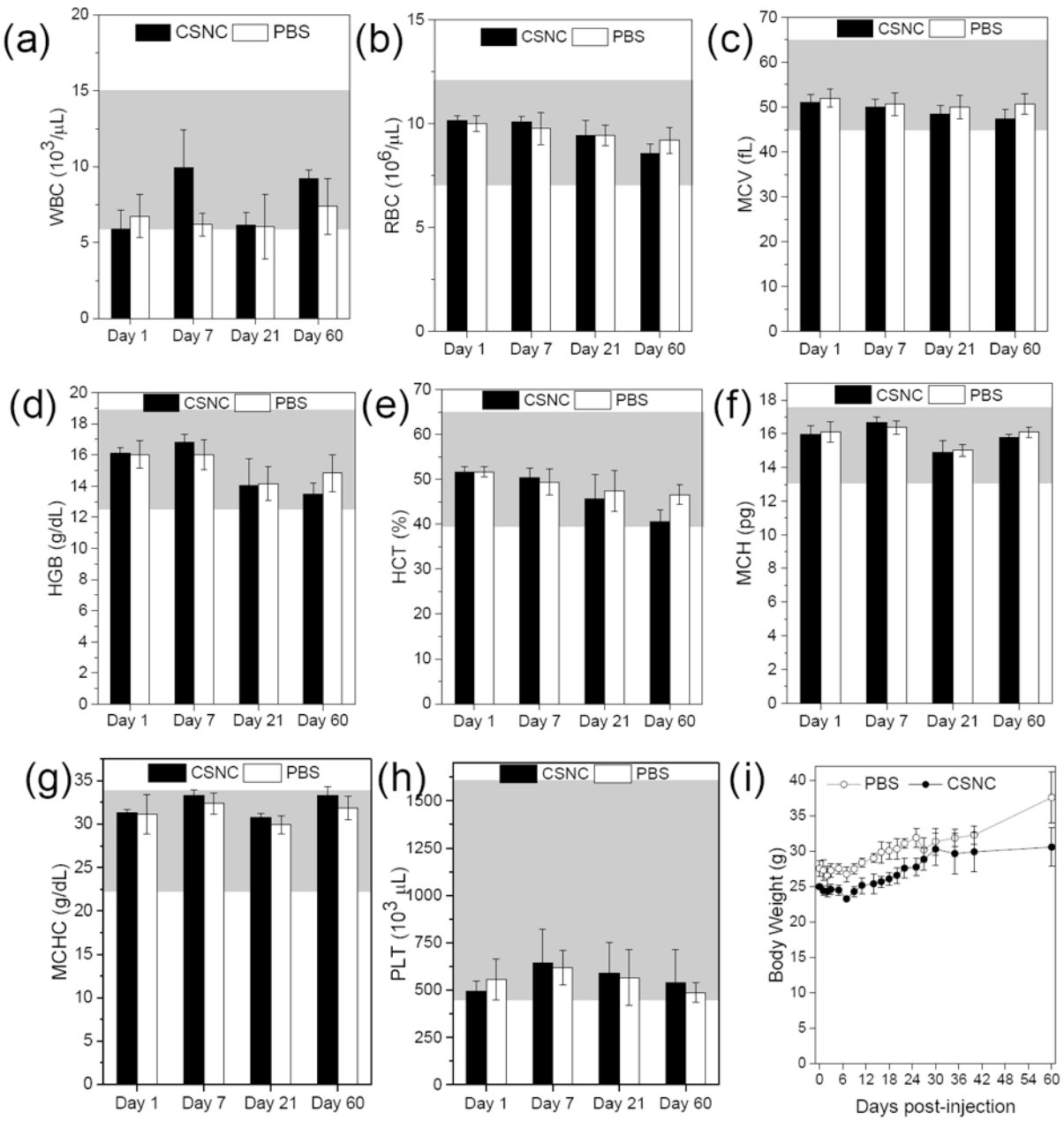

Figure 4. Long term toxicity assessment *in vivo*

Complete hematology data (a) white blood cell, (b) red blood cell, (c) mean corpuscular volume, (d) hemoglobin, (e) hematocrit, (f) mean corpuscular hemoglobin, (g) mean corpuscular hemoglobin concentration, and (h) platelet, collected at day 1, 7, 21 and 60 from female ICR CD-1 mice injected with therapeutic dose of CSNC (30 mg kg^{-1}) or PBS (n = 3). Grey regions represent normal range of the hematology parameters in female ICR mice. (i) Body weight measurements over a period of 60 days. Data is presented as mean ± SD.

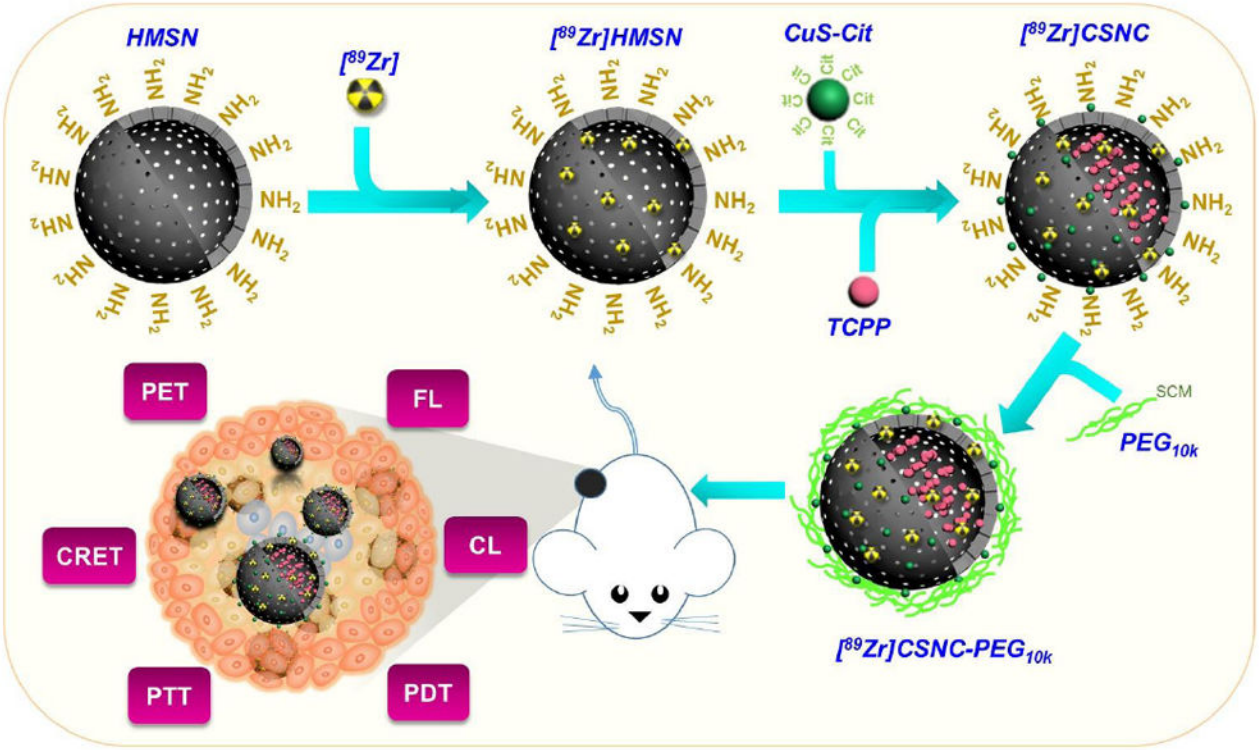

Scheme 1.

Schematic illustration for the self-assembly of radiolabeled core-satellite nanoconstructs (CSNC) for simultaneous positron emission tomography (PET), fluorescence (FL), Cerenkov luminescence (CL) and Cerenkov resonance energy transfer(CRET) imaging and synergistic photothermal (PTT) and photodynamic therapy (PDT) in breast tumor-bearing mice. CSNCs are prepared by electrostatic interaction-driven self-assembly of [^{89}Zr]-labeled hollow mesoporous silica nanoparticles (HMSN) and citrate-capped CuS nanosatellites, followed by encapsulation of TCPP porphyrin. Branched-PEG is grafted to impart greater colloidal stability and biocompatibility.